STATISTICS, OPTIMIZATION AND INFORMATION COMPUTING
Stat., Optim. Inf. Comput., Vol. **12**, January 2024, pp 267–280.
Published online in International Academic Press (www.IAPress.org)

Hyperspectral Image Restoration Based on Color Superpixel segmentation

Huiying Huang [1], Shaoting Peng [1], Gaohang Yu [2], Jinhong Huang [1], Wenyu Hu [1,*]

[1] *School of Mathematics and Computer Science, Gannan Normal University, Ganzhou 341000, China*
[2] *Department of Mathematics, School of Science, Hangzhou Dianzi University, Hangzhou 310018, China*

Abstract Hyperspectral images (HSI) are often degraded by various types of noise during the acquisition process, such as Gaussian noise, impulse noise, dead lines, and stripes. Recently, there has been growing attention to low-rank matrix / tensor-based methods for HSI data restoration, assuming that the overall data are low-rank. However, this assumption is often inaccurate due to the spatial heterogeneity of local similarity characteristics in HSI. Moreover, traditional cube-based methods involve dividing the HSI into fixed-size cubes, which fails to provide flexible coverage of locally similar regions at varying scales. Inspired by superpixel segmentation, this paper proposes a Shrink Low-rank Super-tensor (SLRST) approach for HSI recovery. Instead of using fixed-size cubes, SLRST employs a size-adaptive super-tensor. The proposed approach is effectively solved by using the Alternating Direction Method of Multipliers (ADMM). Numerical experiments on HSI datasets verify that the proposed method outperforms other competing methods.

Keywords Hyperspectral image, Low rank matrix/tensor completion, Superpixel segmentation, ADMM

AMS 2010 subject classifications. Primary: 68W25, 68W30, Secondary: 65Y04, 65Y10.

DOI: 10.19139/soic-2310-5070-1912

1. Introduction

Hyperspectral images (HSI) are captured by sensors with high spectral resolution and consist of hundreds of adjacent narrow spectral band images [1]. Due to the abundance of spectral information they provide, hyperspectral imagery has demonstrated wide applicability across various fields, including geological surveying, urban planning, aviation, and agriculture. Although hyperspectral imagery is highly useful, HSI often suffers from various types of noise. Noise can not only reduce the visual quality of an image, but also significantly impede the accuracy of subsequent computational and analytical operations, such as spectral unmixing [2], target detection [3], image classification [4] and super-resolution [5]. As a result, the recovery of hyperspectral images has become a critical and difficult research area.

Over the past two decades, numerous approaches to denoising HSI have been proposed [6, 7, 8, 9, 10, 11, 14, 15, 16, 17, 18]. Many of these techniques make use of traditional image denoising methods by treating each spectral band of the HSI as a grayscale image [6] or by considering each pixel across all spectral bands as a signal [7]. However, these denoising techniques do not take into account the correlations between different spectral bands or adjacent pixels, which can lead to suboptimal recovery results. To address the correlations among all spectral information and achieve better removal of mixed noises, Yang et al. [8] unfolded the HSI into a matrix and proposed a novel model that combines collaborative total variation and cyclic regularization. Nevertheless, the operation of matrix unfolding destroys the multidimensional structure of the HSI data.

[*] Correspondence to: Wenyu Hu (Email: cswenyuhu@163.com). School of Mathematics and Computer Science, Gannan Normal University, Ganzhou 341000, China.

ISSN 2310-5070 (online) ISSN 2311-004X (print)

To preserve the multidimensional structure and take into account the correlations on individual modes of the HSI, tensor-based approaches [9, 10, 11] have been gaining considerable attention due to their capacity to capture the intrinsic structure of tensors. Kilmer et al. [12, 13] first proposed tensor singular value decomposition (t-SVD) based on tensor-tensor products. These methods process tensors as a whole without matrixization or unfolding, thus avoiding the loss of intrinsic structural information. As a result, Lu et al. [14] extended the matrix nuclear norm to introduce the tensor nuclear norm (TNN). They assumed that high-dimensional images usually have a low-rank structure as a whole, and applied the TNN to denoise color images and videos, leading to promising recovery results. Nevertheless, due to the complex local similarity characteristics exhibited by HSI, this assumption is not always valid.

In order to address the issues mentioned above, fixed-sized cubes are often used as a universal unit for representing tensor data. Three-dimensional cube-based methods [15, 16, 17] employ a fixed-sized slider as a local probe to divide the HSI data into multiple blocks with the same dimensions. Subsequently, these methods carry out low rank tensor approximation analysis on each individual block. Establishing the size of the slider can be difficult as the low rank assumption may not be valid within large segmented blocks. While using smaller cubes can better capture local similarity, it can also lead to increased computational complexity. Furthermore, manually setting different slider sizes for different HSI data can significantly increase the time cost.

Jiang et al. [18] proposed a low-rank tensor approximation model to tackle the issue of HSI data. This approach involves using superpixel segmentation on the smooth band of the HSI data. The irregular blocks resulting from segmentation are then expanded into regular blocks, known as super-tensors. A low-rank tensor approximation is then applied to each super-tensor. However, it should be noted that smooth bands only contain spectral intensity and such simple block filling will increase the rank of super-tensors. This paper proposes an HSI restoration model based on color superpixel segmentation. The technique of shrinking irregular blocks is used to extract the super-tensor, which preserves the low rank property of the obtained super-tensors.

2. Preliminaries

In this section, we introduce some notations used later and then give a brief review of the t-SVD.

2.1. Notations

Throughout this paper, we uniformly use calligraphic letters, capital letters, boldface lowercase letters, and non-bold lowercase letters to denote tensors, matrices, vectors, and scalars, respectively. For example, a tensor $\mathcal{A}$, a matrix $\mathbf{A}$, a vector $\mathbf{a}$, and a scalar a. We have summarized some other notations used in this paper in Table 1.

Table 1. Notation declarations

Notation	Explanation
$\mathbf{A}^{(i)}$	The i-th frontal slice of a third-order tensor $\mathcal{A}$.
$\mathcal{A}(i_1, i_2, i_3)$	The (i_1, i_2, i_3)-th element of a third-order tensor $\mathcal{A}$.
$\mathcal{A}(i_1, i_2, :)$	The (i_1, i_2)-th tube of a third-order tensor $\mathcal{A}$.
$\|\mathcal{A}\|_1 = \sum_{i_1,i_2,i_3} \lvert\mathbf{a}_{i_1,i_2,i_3}\rvert$	The ℓ_1 norm of a third-order tensor $\mathcal{A}$.
$\|\mathcal{A}\|_F = (\sum_{i_1,i_2,i_3} \lvert\mathbf{a}_{i_1,i_2,i_3}\rvert^2)^{\frac{1}{2}}$	The Frobenius norm of a third-order tensor $\mathcal{A}$.

2.2. Tensor singular value decomposition

Definition 2.1 (Fast Fourier Transform [14])
For $\mathcal{X} \in \mathbb{R}^{n_1 \times n_2 \times n_3}$, $\bar{\mathcal{X}} = \mathit{fft}(\mathcal{X}, [], 3)$ means performing Fast Fourier Transform on all tubes along the third dimension of $\mathcal{X}$. The *fft* is a **Matlab** command, and $\mathcal{X} = \mathit{ifft}(\bar{\mathcal{X}}, [], 3)$, *ifft* represents the inverse Fast Fourier Transform.

Definition 2.2 (t-product [12])
The t-product of $\mathcal{A} \in \mathbb{R}^{n_1 \times n_2 \times n_3}$ and $\mathcal{B} \in \mathbb{R}^{n_2 \times l \times n_3}$, denoted as $\mathcal{C} = \mathcal{A} * \mathcal{B} \in \mathbb{R}^{n_1 \times l \times n_3}$, and is given by

$$\mathcal{C}(i, j, :) = \sum_{k=1}^{n_2} \mathcal{A}(i, k, :) \circ \mathcal{B}(k, j, :).$$

where $\circ$ denotes the circular convolution between two tubes.

Definition 2.3 (Identity tensor [12])
The identity tensor $\mathcal{I} \in \mathbb{R}^{n_1 \times n_1 \times n_3}$ is a tensor whose first frontal slice is the $n_1 \times n_1$ identity matrix and all other frontal slices are zero.

Definition 2.4 (Orthogonal tensor [12])
A tensor $\mathcal{X} \in \mathbb{R}^{n_1 \times n_1 \times n_3}$ is orthogonal if

$$\mathcal{X}^\top * \mathcal{X} = \mathcal{X} * \mathcal{X}^\top = \mathcal{I}.$$

Definition 2.5 (f-diagonal tensor [12])
A tensor is called f-diagonal if each of its frontal slices is diagonal matrix.

Theorem 2.1 (t-SVD [13, 14])
Let $\mathcal{X} \in \mathbb{R}^{n_1 \times n_2 \times n_3}$. The t-SVD of $\mathcal{X}$ is given as follows:

$$\mathcal{X} = \mathcal{U} * \mathcal{S} * \mathcal{V}^\top,$$

where $\mathcal{U} \in \mathbb{R}^{n_1 \times n_1 \times n_3}$, $\mathcal{V} \in \mathbb{R}^{n_2 \times n_2 \times n_3}$ are orthogonal tensors, and $\mathcal{S} \in \mathbb{R}^{n_1 \times n_2 \times n_3}$ is a f-diagonal tensor. Figure 1 illustrates the decomposition.

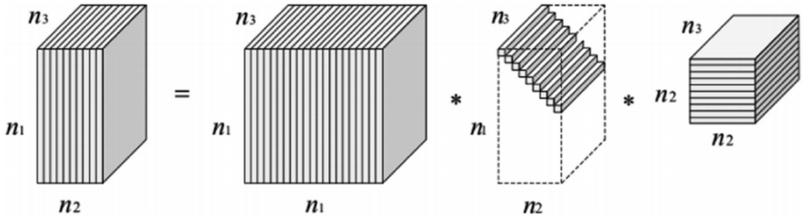

Figure 1. The t-SVD of an $n_1 \times n_2 \times n_3$ tensor.

Definition 2.6 (Tensor tubal rank [14])
For $\mathcal{X} \in \mathbb{R}^{n_1 \times n_2 \times n_3}$, the tensor tubal rank of $\mathcal{X}$, denoted as $rank_t(\mathcal{X})$, and is defined as the number of non-zero singular tubes of $\mathcal{S}$, that is

$$rank_t(\mathcal{X}) \triangleq \sharp\{i, \mathcal{S}(i, i, :) \neq 0\},$$

where $\mathcal{S}$ is from the t-SVD of $\mathcal{X} = \mathcal{U} * \mathcal{S} * \mathcal{V}^\top$. The symbol $\sharp$ represents the number of i satisfying $\mathcal{S}(i, i, :) \neq 0$.

Definition 2.7 (TNN [14])
For $\mathcal{X} = \mathcal{U} * \mathcal{S} * \mathcal{V}^\top$, its TNN is defined as

$$\|\mathcal{X}\|_* \triangleq < \mathcal{S}, \mathcal{I} > = \sum_{i=1}^{r} \mathcal{S}(i, i, :),$$

where $r = rank_t(\mathcal{X})$.

3. Relate works

During the acquisition and transmission processes, HSI is susceptible to be corrupted by various types of noise. In the face of such contamination, the degradation model for an observation $\mathcal{Y} \in \mathbb{R}^{n\times m\times b}$ can be formulated as follows:

$$\mathcal{Y} = \mathcal{X} + \mathcal{E}, \tag{1}$$

where $\mathcal{Y} \in \mathbb{R}^{n\times m\times b}$ represents the noisy HSI data, $\mathcal{X} \in \mathbb{R}^{n\times m\times b}$ represents the clean HSI data, and $\mathcal{E} \in \mathbb{R}^{n\times m\times b}$ represents sparse noise. m, n, and b denote height, width, and spectrum number, respectively. To address the problem Eq. (1), Lu et al. [14] treating multi-dimensional images as being in the overall low rank and introduced a approach based on TNN

$$\begin{aligned} &\min_{\mathcal{X},\mathcal{E}} \|\mathcal{X}\|_* + \lambda\|\mathcal{E}\|_1 \\ &s.t.\ \mathcal{Y} = \mathcal{X} + \mathcal{E}, \end{aligned} \tag{2}$$

where $\|\mathcal{X}\|_*$ defines the TNN of $\mathcal{X}$, $\|\mathcal{E}\|_1$ defines the ℓ_1 norm of $\mathcal{E}$, $\lambda > 0$ is a trade-off parameter.

In problem (2), it is assumed that the underlying data is holistic low-rank. However, this assumption may not hold true for HSI data due to the presence of spatial diversity. To tackle this challenge, Jiang et al. [18] proposed a tensor-based low-rank approximation model for multimedia data recovery, which incorporates the use of superpixel segmentation. Prior to carrying out the superpixel segmentation, they preprocess the multi-dimensional data $\mathcal{Y} \in \mathbb{R}^{n\times m\times b}$ by generating the smooth band image

$$Y_{smooth} = \frac{1}{b}\sum_{i=1}^{b} \mathbf{Y}^{(i)}.$$

To carry out the superpixel segmentation, they utilize Y_{smooth} as the reference and partition the noisy data into K irregularly-shaped superpixels. Next, they identify the envelope cube of each superpixel and replace the missing pixels with the original pixels, while also labeling the envelope cube as the i-th super-tensor. Low-rank approximation is then performed on these super-tensors to attain high-dimensional image denoising. The model is described as follows:

$$\begin{aligned} &\min_{\mathcal{X},\mathcal{E}} \sum_{i=1}^{K} \frac{1}{\mu_i}\Psi(R_i\mathcal{X}) + \lambda\|\mathcal{E}\|_1 \\ &s.t.\ \mathcal{Y} = \mathcal{X} + \mathcal{E}, \end{aligned}$$

where R_i is the operator to get the i-th super-tensor, $R_i\mathcal{X}$ represents the size-adaptive super-tensor for the i-th superpixel, $\Psi(\cdot)$ is low-rank tensor regularization, and μ_i and λ are regularization parameters.

However, there is a problem in using the smoothed band Y_{smooth}, which is a grayscale image for superpixel segmentation. This approach may only leads to visually similar blocks based on intensity and may not accurately represent the local similarity of the HSI. Moreover, the approach of extending superpixel blocks in constructing super-tensors has the potential to disrupt the low-rank tendency of the local data.

4. The proposed method

In this section, we propose a novel shrink low-rank super-tensor (SLRST) model for HSI recovery. The SLRST model integrates color superpixel segmentation to ensure content similarity within the extracted superpixel blocks. Furthermore, we utilize a pixel shrinking operation to construct super-tensors and preserve their low-rank properties.

4.1. *Color image superpixel segmentation*

HSI data is composed of numerous spectral bands, which contribute to a rich color representation in the resulting image. Each band in HSI can be considered as a grayscale image, and the smoothed band, denoted as Y_{smooth}, acts as the smoothness component for all bands. Similarly, Y_{smooth} is also a grayscale image.

In Figure 2 (c), superpixel segmentation is applied to Y_{smooth}. Though the resulted pixel blocks show visual similarity in terms of intensity, it can be seen that the pixel segmentation only based on gray intensity might not force adjacent pixels with similar content (see Figure 2 (b)) to be in the same block (see Figure 2 (c)). This limitation in grayscale image superpixel segmentation approach highlights the need for additional techniques to ensure that all pixels with similar content are included in the same block during the restoration process of HSI data.

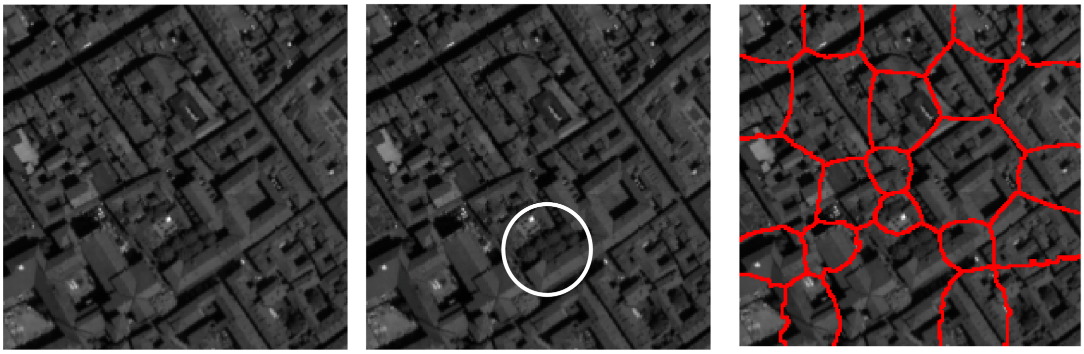

(a) Y_{smooth} (b) Y_{smooth} content-similar pixels (c) superpixel segmentation on Y_{smooth}

Figure 2. Superpixel segmentation of smooth grayscale images.

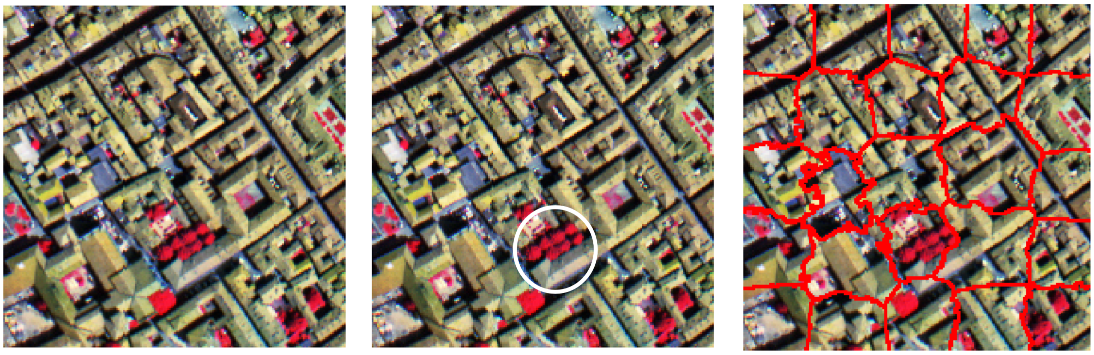

(a) Y_{color} (b) Y_{color} content-similar pixels (c) superpixel segmentation on Y_{color}

Figure 3. Superpixel segmentation of false color images.

To extract content-similar blocks in the HSI data, we first extract information from all spectral bands of HSI using MATLAB's hyperspectral toolbox. We then apply false-color mapping to this information, generating a three-channel color image, denoted as Y_{color}. Superpixel segmentation is performed on Y_{color} to obtain the segmentation result as shown in Figure 3 (c).

The white circles in Figure 2 (b) and Figure 3 (b) show pixels with similar content in HSI data. Comparing Figure 2 (c) with Figure 3 (c), it is evident that Y_{color} has better accuracy in segmenting content-similar pixels into one block, implying that the superpixel segmentation result of Y_{color} is mcuh closer to the ground truth.

4.2. Shrink low-rank super-tensor

After performing superpixel segmentation on Y_{color}, we obtain q irregular superpixel blocks. Instead of pixel extension as in [18], we use a shrinkage operation by subdivide some large irregular superpixel blocks into multiple small regular pixel blocks. This process helps preserve the low-rank property of local blocks and prevents overlapping pixels between the segmented blocks. The Figure 4 illustrates the specific shrinking effect. From Figure 4, it is evident that the contraction of the i-th irregular superpixel block yields n_i regular superpixel blocks. As a result, all irregular block yields $K = \sum_{i=1}^{q} n_i$ regular superpixel blocks via the contraction process, leading to the production of K contraction super-tensors.

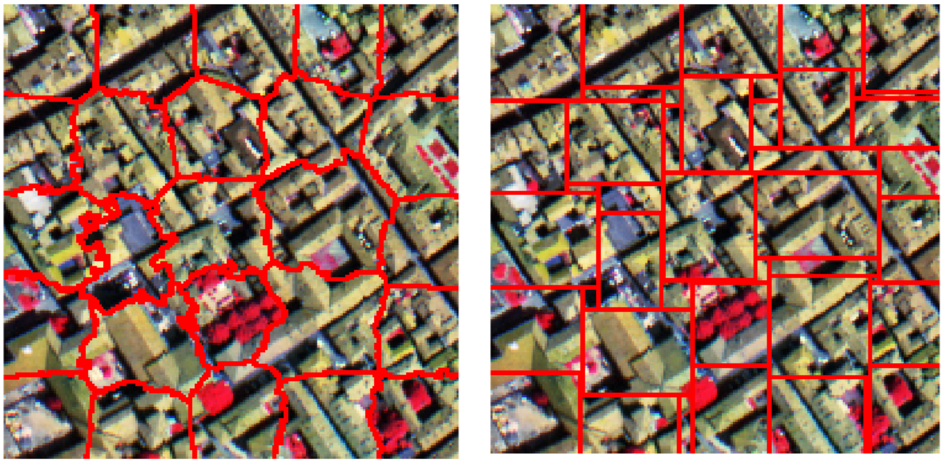

(a) Irregular superpixel blocks

(b) Regular superpixel blocks

Figure 4. Shrinking 25 irregular superpixel blocks resulted in 46 regular blocks.

Given that each super-tensor is influenced by its surrounding environment, we propose incorporating all super-tensors into a single model and introducing low-rank prior to regularize each super-tensor. The formulation of the proposed SLRST model for HSI data recovery is written as follows:

$$\begin{aligned} &\min_{\mathcal{X},\mathcal{E}} \sum_{i=1}^{K} \frac{1}{\mu_i} \Psi(\Upsilon_i \mathcal{X}) + \lambda \|\mathcal{E}\|_1 \\ &s.t.\ \mathcal{Y} = \mathcal{X} + \mathcal{E}, \end{aligned} \tag{3}$$

where Υ_i is the operator to get the i-th shrink super-tensor, $\Upsilon_i \mathcal{X}$ represents the i-th shrink super-tensor.

To solve the proposed model (3), we adopt the ADMM algorithm. Specifically, by introducing auxiliary variables $\mathcal{M}_i (i = 1, 2, \ldots, K)$, the optimization problem (3) can be transformed to be

$$\begin{aligned} &\min_{\mathcal{X},\mathcal{E},\mathcal{M}_i} \sum_{i=1}^{K} \frac{1}{\mu_i} \Psi(\mathcal{M}_i) + \lambda \|\mathcal{E}\|_1 \\ &s.t.\ \mathcal{Y} = \mathcal{X} + \mathcal{E}, \\ &\quad \mathcal{M}_i = \Upsilon_i \mathcal{X}. \end{aligned} \tag{4}$$

Then, the augmented Lagrangian function of (4) is

$$\begin{aligned} L(\mathcal{M}_i, \mathcal{X}, \mathcal{E}, \mathcal{P}_i, \mathcal{Z}) = &\sum_{i=1}^{K}\{\frac{1}{\mu_i}\Psi(\mathcal{M}_i) + \frac{\beta}{2}\|\Upsilon_i\mathcal{X} - \mathcal{M}_i + \frac{\mathcal{P}_i}{\beta}\|_F^2\} \\ &+ \lambda\|\mathcal{E}\|_1 + \frac{\rho}{2}\|\mathcal{Y} - \mathcal{X} - \mathcal{E} + \frac{\mathcal{Z}}{\rho}\|_F^2. \end{aligned} \tag{5}$$

where $\mathcal{P}_i \in \mathbb{R}^{n\times m\times b}$ and $\mathcal{Z} \in \mathbb{R}^{n\times m\times b}$ are Lagrangian multipliers and $\beta > 0$ and $\rho > 0$ are penalty parameters. Under the framework of ADMM, the proposed algorithm has the following iteration scheme:

$$\begin{cases} \mathcal{M}_i^{c+1} = arg\min_{\mathcal{M}_i} L(\mathcal{M}_i, \mathcal{X}^c, \mathcal{E}^c, \mathcal{P}_i^c, \mathcal{Z}^c), \\ \mathcal{E}^{c+1} = arg\min_{\mathcal{E}} L(\mathcal{M}_i^{c+1}, \mathcal{X}^c, \mathcal{E}, \mathcal{P}_i^c, \mathcal{Z}^c), \\ \mathcal{X}^{c+1} = arg\min_{\mathcal{X}} L(\mathcal{M}_i^{c+1}, \mathcal{X}, \mathcal{E}^{c+1}, \mathcal{P}_i^c, \mathcal{Z}^c), \\ \mathcal{Z}^{c+1} = \mathcal{Z}^c + \rho(\mathcal{Y} - \mathcal{X}^{c+1} - \mathcal{E}^{c+1}), \\ \mathcal{P}_i^{c+1} = \mathcal{P}_i^c + \beta(\Upsilon_i\mathcal{X}^{c+1} - \mathcal{M}_i^{c+1}). \end{cases} \tag{6}$$

where the superscript c denotes the iteration index. Next, we show the details of each subproblem.

1) $\mathcal{M}_i$-subproblem: Fix other variables and solve the subproblem of $\{\mathcal{M}_i\}_{i=1}^K$ as follows:

$$\mathcal{M}_i^{c+1} = arg\min_{\mathcal{M}_i}\sum_{i=1}^{K}\{\frac{1}{\mu_i}\Psi(\mathcal{M}_i) + \frac{\beta}{2}\|\Upsilon_i\mathcal{X}^c - \mathcal{M}_i + \frac{\mathcal{P}_i^c}{\beta}\|_F^2\}. \tag{7}$$

Introducing the TNN, the convex relaxation of the tensor tubal rank, i.e., $\Psi(\mathcal{M}_i) = \|\mathcal{M}_i\|_*$, Eq. (7) can be separated into K subproblems as follows:

$$\mathcal{M}_i^{c+1} = arg\min_{\mathcal{M}_i}\frac{1}{\mu_i}\|\mathcal{M}_i\|_* + \frac{\beta}{2}\|\mathcal{M}_i - (\Upsilon_i\mathcal{X}^c + \frac{\mathcal{P}_i^c}{\beta})\|_F^2.$$

According to the tensor singular value thresholding (t-SVT) operator [14], the closed-form solution of $\mathcal{M}_i$ is

$$\mathcal{M}_i^{c+1} = \mathcal{U} * \mathcal{S}^+ * \mathcal{V}^\top, \tag{8}$$

where $\mathcal{S}$ is from the t-SVD of $\Upsilon_i\mathcal{X}^c + \frac{\mathcal{P}_i^c}{\beta} = \mathcal{U} * \mathcal{S} * \mathcal{V}^\top$ and $\mathcal{S}^+ = \mathit{ifft}(max(\bar{\mathcal{S}} - \frac{1}{\beta\mu_i}, 0), [], 3)$.

2) $\mathcal{E}$-subproblem: Fix other variables and solve the subproblem of $\mathcal{E}$ as follows:

$$\mathcal{E}^{c+1} = arg\min_{\mathcal{E}}\lambda\|\mathcal{E}\|_1 + \frac{\rho}{2}\|\mathcal{E} - (\mathcal{Y} - \mathcal{X}^c + \frac{\mathcal{Z}^c}{\rho})\|_F^2. \tag{9}$$

The closed-form solution of (9) is given by:

$$\mathcal{E}^{c+1} = S_{\frac{\lambda}{\rho}}(\mathcal{Y} - \mathcal{X}^c + \frac{\mathcal{Z}^c}{\rho}), \tag{10}$$

where $S_{\frac{\lambda}{\rho}}(\cdot)$ is the soft-thresholding operator in the form of

$$S_{\frac{\lambda}{\rho}}(x) = \begin{cases} x - \frac{\lambda}{\rho},\ if\ x > \frac{\lambda}{\rho}, \\ x + \frac{\lambda}{\rho},\ if\ x < \frac{\lambda}{\rho}, \\ 0,\ otherwise. \end{cases}$$

3) $\mathcal{X}$-subproblem: Fix other variables and solve the subproblem of $\mathcal{X}$ as follows:

$$\mathcal{X}^{c+1} = arg\min_{\mathcal{X}} \sum_{i=1}^{K} \{\frac{\beta}{2}\|\Upsilon_i\mathcal{X} - (\mathcal{M}_i^{c+1} - \frac{\mathcal{P}_i^c}{\beta})\|_F^2\} + \frac{\rho}{2}\|\mathcal{X} - (\mathcal{Y} - \mathcal{E}^{c+1} + \frac{\mathcal{Z}^c}{\rho})\|_F^2. \tag{11}$$

Taking the derivative of Eq. (11) with respect to $\mathcal{X}$ and setting to zero, we then update $\mathcal{X}$ as

$$\mathcal{X}^{c+1} = [\rho(\mathcal{Y} - \mathcal{E}^{c+1} + \frac{\mathcal{Z}^c}{\rho}) + \beta\sum_{i=1}^{K}\Upsilon_i^{-1}(\mathcal{M}_i^{c+1} - \frac{\mathcal{P}_i^c}{\beta})] \oslash (\rho\mathcal{J} + \beta\sum_{i=1}^{K}\Upsilon_i^{-1}\Upsilon_i), \tag{12}$$

where $\oslash$ represents the element-wise division, $\mathcal{J} \in \mathbb{R}^{n\times m\times b}$ is the all-ones tensor.

To sum up, the subproblems of $\mathcal{M}_i$, $\mathcal{E}$, and $\mathcal{X}$ have closed-form solutions and the overall algorithm for solving SLRST model can be summarized in Algorithm 1.

Algorithm 1 SLRST

```
Input: The noise data $\mathcal{Y}$
Output: $\mathcal{X}$
Initialize: $\mathcal{M}_i^{(0)} = \mathcal{E}^{(0)} = \mathcal{X}^{(0)} = \mathcal{Z}^{(0)} = \mathcal{P}_i^{(0)}$, regularization parameters $\lambda$, $\mu_i$, penalty parameters $\beta$, $\rho$, and $c_{max} = 200$.
while not converge do
    Update $\mathcal{M}_i (i = 1, 2, \ldots, K)$ by Eq. (8);
    Update $\mathcal{E}$ by Eq. (10);
    Update $\mathcal{X}$ by Eq. (12);
    Update $\mathcal{P}_i$, $\mathcal{Z}$ by Eq. (6);
    $\rho \leftarrow 1.1\rho$.
    Check the convergence condition: $(\|\mathcal{X}^{c+1} - \mathcal{X}^c\|_F^2/\|\mathcal{X}^c\|_F^2) < 10^{-5}$
end while
```

5. Experiments

This section verifies the effectiveness of the proposed SLRST algorithm in HSI data restoration.

5.1. *Evaluation metrics*

In this paper, the peak signal-to-noise ratio (PSNR) index and the structural similarity (SSIM) index are used for quantitative evaluation of the restoration results. For an HSI, the PSNR and SSIM values are calculated between each clean band and its corresponding restored band. These values are then averaged, resulting in the mean PSNR (MPSNR) and mean SSIM (MSSIM) indices. The definitions of these indices are as follows:

$$\begin{aligned}
\mathrm{PSNR}_i &= 10 * \log_{10}\frac{mn}{\sum_{x=1}^{m}\sum_{y=1}^{n}[\hat{u}_i(x,y) - u_i(x,y)]^2},\\
\mathrm{SSIM}_i &= \frac{(2\mu_{u_i}\mu_{\hat{u}_i} + C_1)(2\sigma_{u_i}\mu_{\hat{u}_i} + C_2)}{(\mu_{u_i}^2\mu_{\hat{u}_i}^2 + C_1)(\sigma_{u_i}^2 + \sigma_{\hat{u}_i}^2 + C_2)},\\
\mathrm{MPSNR} &= \frac{1}{b}\sum_{i=1}^{b}\mathrm{PSNR}_i,\\
\mathrm{MSSIM} &= \frac{1}{b}\sum_{i=1}^{b}\mathrm{SSIM}_i,
\end{aligned}$$

where u_i and $\hat{u}_i$ represent the i-th bands of the reference image and the restored image, respectively. μ_{u_i} and $\mu_{\hat{u}_i}$ denote the average values of the images u_i and $\hat{u}_i$, while σ_{u_i} and $\sigma_{\hat{u}_i}$ represent the variances, and $\sigma_{u_i\hat{u}_i}$ is the covariance between u_i and $\hat{u}_i$. Generally speaking, better restoration results are reflected by higher SSIM and PSNR values.

5.2. *Experimental setup*

During the simulation process, salt and pepper noise was randomly added to all bands of the test datasets, with noise densities of p=10%, p=20%, and p=30%. The performance of the SLRST algorithm was then compared with three classic tensor data recovery algorithms: RPCA [19], SNN [20], and TNN [14].

In our experiments, the parameters are set to the values at which each method can achieve its best results. All experiments are implemented by MATLAB R2020b software on a PC with Intel(R) Core(TM) i5-7200U 2.70 GHz CPU and 4.00 GB RAM.

5.3. *Parameter choice and convergence analysis*

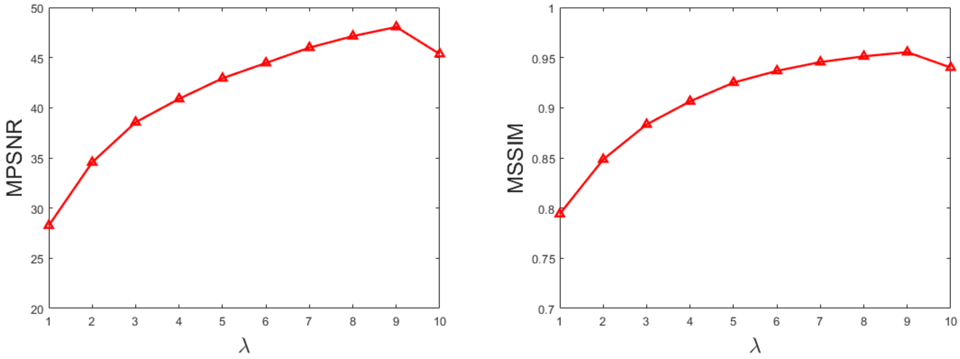

(a) MPSNR

(b) MSSIM

Figure 5. Sensitivity analysis of parameter λ by using SLRST.

The SLRST involves 2 parameters, including $\mu_i(i = 1, 2, \ldots, K)$ and λ. We set $\mu_i = 1/\sqrt{(min(n_i, m_i)b)}$, which is related to the size of the i-th super-tensor $\Upsilon_i\mathcal{X} \in \mathbb{R}^{n_i\times m_i\times b}$ and refers to Theorem 4.1 in [14]. The parameter λ is used to balance the low-rank term and the sparse term in the SLRST. Figure 5 illustrates the MPSNR and MSSIM of the Indian Pines dataset with 10% density salt and pepper noise. Our method was applied with various values of $\lambda(\lambda = 1, 2, \ldots, 10)$. The MPSNR and MSSIM values reach their maximum when $\lambda = 9$. Therefore, we set $\lambda = 9$ for subsequent experiments. To demonstrate the convergence performance of SLRST, we plot the curves that represent changes in the values of our objective function with respect to the number of iterations in Figure 6. It is evident from the plot that the proposed SLRST algorithm converges quickly.

5.4. *Indian Pines dataset*

In this subsection, we conducted simulated experiments using the Indian Pines dataset [21]. The dataset was collected by the AVIRIS sensor over the Indian Pines test site in northwestern Indiana. To prepare the data, we excluded bands that cover the region of water absorption, resulting in a reduced number of bands to 200. The size of the subimage was chosen as $145 \times 145 \times 200$.

Salt and pepper noise was randomly added to all bands (200 bands) of the Indian Pines dataset, with noise densities of p=10%, p=20%, and p=30%. The MPSNR and MSSIM values generated by all competing algorithms are presented in Table 2. From the table, it is apparent that regardless of the salt and pepper noise density used, SLRST consistently achieves the highest MPSNR and MSSIM scores most of the time. This observation confirms the effectiveness of our proposed method.

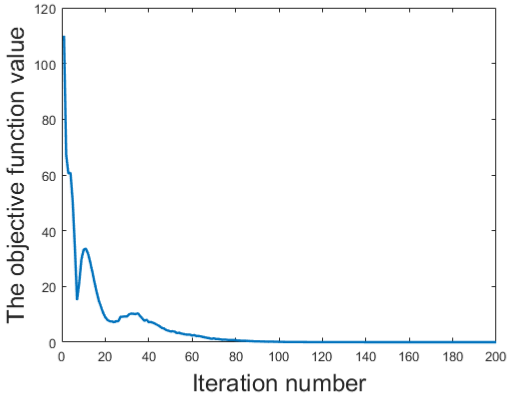

Figure 6. Convergence behavior.

Table 2. Quantitative comparison of all methods on the Indian Pines dataset under salt and pepper noise densities of p=10%, p=20%, and p=30%.

Nosie Density	p=10%		p=20%		p=30%	
Index	MPSNR	MSSIM	MPSNR	MSSIM	MPSNR	MSSIM
RPCA	16.94	0.4282	9.91	0.4298	6.89	0.4317
SNN	37.68	0.8905	33.81	0.8002	30.91	0.7105
TNN	30.91	0.8458	25.12	0.6198	21.80	0.4708
SLRST	**47.14**	**0.9513**	**44.26**	**0.9437**	**40.53**	**0.9303**

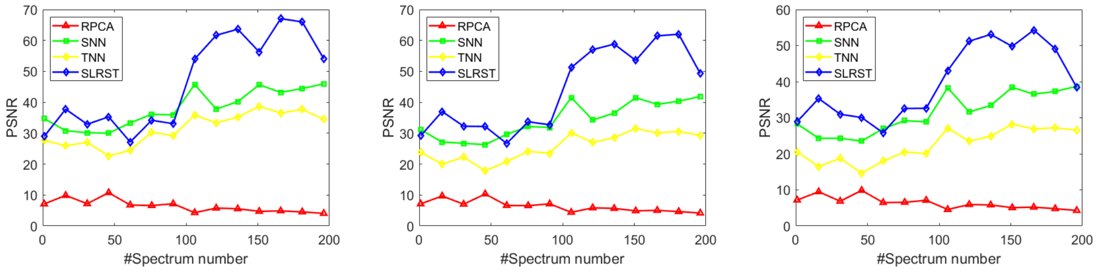

(a) p=10%
(b) p=20%
(c) p=30%

Figure 7. PSNRs obtained at salt and pepper noise densities of p=10%, p=20%, and p=30% by the compared methods: RPCA, SNN, TNN and SLRST.

The PSNR and SSIM values for each band are depicted in Figure 7 and Figure 8, respectively. The results are the average PSNR and SSIM values obtained after 10 experiments. Due to the random addition of salt and pepper noise in each band and the varying intensity of each band, the calculated PSNR and SSIM values for each band are inconsistent. Therefore, it can be seen that the curves of all methods have significant fluctuations. Even then, it is evident from both figures that the curves obtained by SLRST consistently exhibit the highest PSNR and SSIM values compared to the competing methods. This observation further emphasizes the superior performance of SLRST.

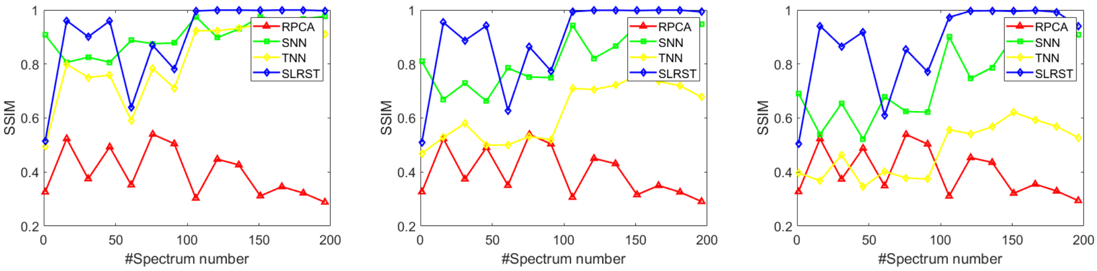

(a) p=10% (b) p=20% (c) p=30%

Figure 8. SSIMs obtained at salt and pepper noise densities of p=10%, p=20%, and p=30% by the compared methods: RPCA, SNN, TNN and SLRST.

5.5. *Pavia city center dataset*

In this subsection, we conducted simulated experiments using the Pavia city center dataset [22]. The ROSIS-03 Reflective Optics System Imaging Spectrometer was used to collect the dataset. Unfortunately, the Pavia city center dataset had a lot of noise, making some of the spectral bands unusable for denoising. Consequently, the first 22 bands, which contained all the noisy bands, were removed. The size of the subimage was set to 200 × 200 × 80, as illustrated in Figure 9.

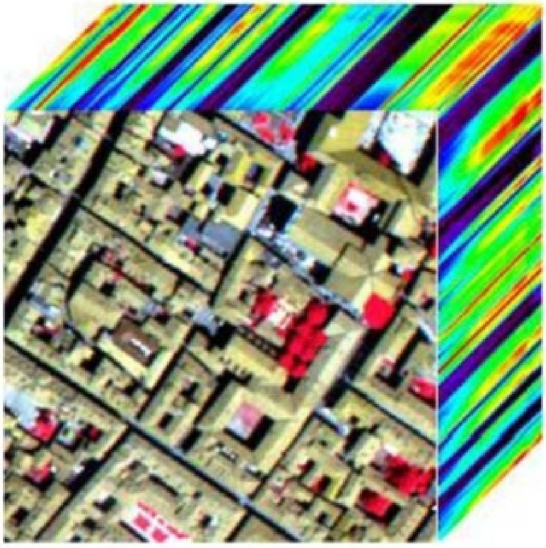

Figure 9. Pavia city center dataset.

Salt and pepper noise was randomly added to all bands (80 bands) of the Pavia city center dataset, with noise densities of p=10%, p=20%, and p=30%. The MPSNR and MSSIM values generated by different competing algorithms are summarized in Table 3. As observed from the table, the SLRST algorithm proposed in this paper consistently outperforms the other algorithms in terms of MPSNR and MSSIM values across HSI data with varying densities of salt and pepper noise. These results unequivocally demonstrate the excellent recovery performance of our proposed algorithm.

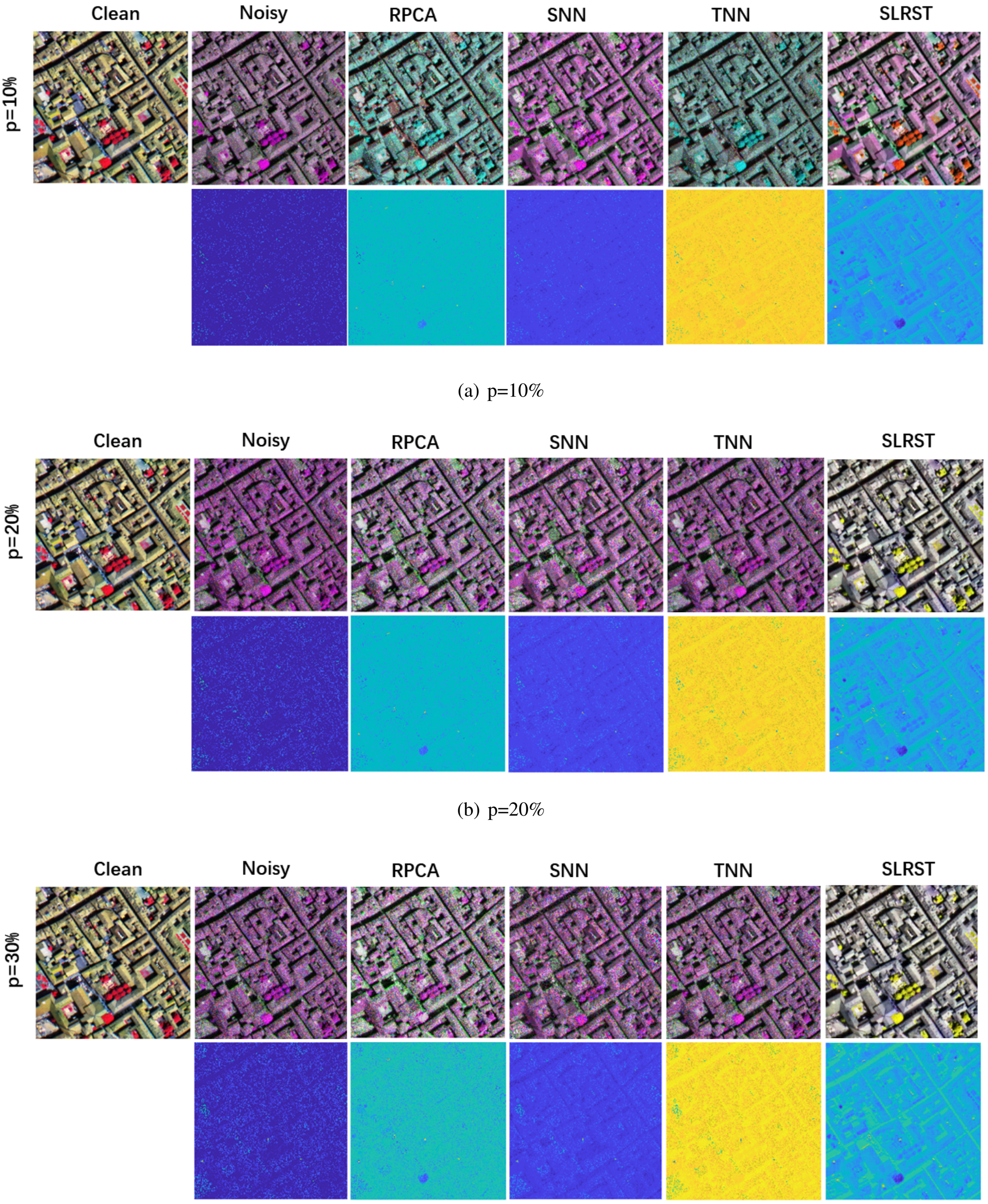

(a) p=10%

(b) p=20%

(c) p=30%

Figure 10. Recovery results and residual images under salt and pepper noise densities of p=10%, p=20%, and p=30% by all methods.

To enhance visual contrast, false-color mapping is employed on all HSI data restored by the algorithm. Additionally, residual images are created by comparing the restored images with the original images. Figure 10

Table 3. Quantitative comparison of all methods on the Pavia city center dataset under salt and pepper noise densities of p=10%, p=20%, and p=30%.

Nosie Density	p=10%		p=20%		p=30%	
Index	MPSNR	MSSIM	MPSNR	MSSIM	MPSNR	MSSIM
RPCA	23.33	0.6878	20.43	0.5728	18.75	0.5156
SNN	29.22	0.8623	25.96	0.7560	23.84	0.6609
TNN	23.14	0.6878	20.19	0.5810	18.45	0.5281
SLRST	**47.14**	**0.9876**	**43.97**	**0.9836**	**38.80**	**0.9731**

shows the results of the visual comparison. It is evident that the recovery result obtained with SLRST is very similar to the original image, demonstrating the algorithm's capability to accurately restore the HSI data. Furthermore, the generated residual images demonstrate a minimal amount of salt and pepper noise, further confirming the dependability of the SLRST in producing precise recovery results.

6. Conclusion

This paper proposes a novel HSI restoration model that utilizes color superpixel segmentation. The proposed model partitions the HSI data into content-similar blocks by performing superpixel segmentation on the false-color channels. These blocks are then compressed to form super-tensors with similar content. Low-rank tensor approximation is then used to denoise the image by preserving the low-rank properties of the divided blocks through shrinkage subdivision. Experimental results on the Indian Pines dataset and the Pavia city dataset demonstrate that the proposed SLRST model achieves the highest MPSNR and MSSIM values, outperforming traditional tensor recovery algorithms.

Acknowledgments

This work was supported by the National Natural Science Foundation of China (Nos. 62266002, 12071104, 82060328 and 12201126), and the Natural Science Foundation of Jiangxi Province, China (No. 20224BAB202004 and 20232BAB206133).

REFERENCES

1. H. Zhang, J. Li, Y. Huang, and L. Zhang, *A nonlocal weighted joint sparse representation classification method for hyperspectral imagery*, IEEE Journal of Selected Topics in Applied Earth Observations and Remote Sensing, vol. 7, no. 6, pp. 2056-2065, 2014.
2. W. He, H. Zhang and L. Zhang, *Total variation regularized reweighted sparse nonnegative matrix factorization for hyperspectral unmixing*, IEEE Transactions on Geoscience and Remote Sensing, vol. 55, no. 7, pp. 3909-3921, 2017.
3. N. M. Nasrabadi, *Hyperspectral target detection : An overview of current and future challenges*, IEEE Signal Processing Magazine, vol. 31, no. 1, pp. 34-44, 2014.
4. F. Luo, L. Zhang, B. Du and L. Zhang, *Dimensionality reduction with enhanced hybrid-graph discriminant learning for hyperspectral image classification*, IEEE Transactions on Geoscience and Remote Sensing, vol. 58, no. 8, pp. 5336-5353, 2020.
5. L. -J. Deng, G. Vivone, W. Guo, M. Dalla Mura and J. Chanussot, *A variational pansharpening approach based on reproducible kernel hilbert space and heaviside function*, IEEE Transactions on Image Processing, vol. 27, no. 9, pp. 4330-4344, 2018
6. X. Liu, S. Bourennane and C. Fossati, *Denoising of hyperspectral images using the PARAFAC model and statistical performance analysis*, IEEE Transactions on Geoscience and Remote Sensing, vol. 50, no. 10, pp. 3717-3724, 2012,.
7. G. Martin, J. M. Bioucas-Dias and A. Plaza, *B-HYCA: Blind hyperspectral compressive sensing*, 2015 IEEE International Geoscience and Remote Sensing Symposium (IGARSS), Milan, Italy, pp. 2856-2859, 2015.
8. M. Yang, Q. Luo, W. Li, M. Xiao, *Nonconvex 3D array image data recovery and pattern recognition under tensor framework*, Pattern Recognition, 122 (108311), 2022.

9. Z. Chen, G. Zhou and Q. Zhao, *Hierarchical factorization strategy for high-order tensor and application to data completion*, IEEE Signal Processing Letters, vol. 28, pp. 1255-1259, 2021.
10. Y. Liu, Z. Long and C. Zhu, *Image completion using low tensor tree rank and total variation minimization*, IEEE Transactions on Multimedia, vol. 21, no. 2, pp. 338-350, 2019.
11. S. Du, B. Liu, G. Shan, Y. Shi, W. Wang, *Enhanced tensor low-rank representation for clustering and denoising*, Knowledge-Based Systems, 243 (108468), 2022.
12. M. E. Kilmer, C. D. Martin, *Factorization strategies for third-order tensors, Linear Algebra and its Applications*, vol. 435, no. 3, pp. 641-658, 2011.
13. M. E. Kilmer, K. Braman, N. Hao, and R. C. Hoover, *Third-order tensors as operators on matrices: A theoretical and computational framework with applications in imaging*, SIAM Journal on Matrix Analysis and Applications, vol. 34, no. 1, pp. 148-172, 2013.
14. C. Lu, J. Feng, Y. Chen, W. Liu, Z. Lin and S. Yan, *Tensor robust principal component analysis with a new tensor nuclear norm*, IEEE Transactions on Pattern Analysis and Machine Intelligence, vol. 42, no. 4, pp. 925-938, 2020.
15. H. Zhang, W. He, L. Zhang, H. Shen and Q. Yuan, *Hyperspectral image restoration using low-rank matrix recovery*, IEEE Transactions on Geoscience and Remote Sensing, vol. 52, no. 8, pp. 4729-4743, 2014.
16. B. Wen, S. Ravishankar and Y. Bresler, *Video denoising by online 3D sparsifying transform learning*, 2015 IEEE International Conference on Image Processing (ICIP), pp. 118-122, 2015.
17. Y.-R. Fan, T.-Z. Huang, *Hyperspectral image restoration via superpixel segmentation of smooth band*, Neurocomputing, 455, pp. 340-352, 2021.
18. Q. Jiang, X.-L. Zhao, J. Lin, Y.-R. Fan, J. Peng, G.-C. Wu, *Superpixel-based robust tensor low-rank approximation for multimedia data recover*, Knowledge-Based Systems, 277 (110812), 2023.
19. E. J. Cands, X. Li, Y. Ma, and J. Wright, *Robust principal component analysis?*, Journal of the ACM (JACM), vol. 58, no. 3, pp. 1-37, 2011.
20. J. Liu, P. Musialski, P. Wonka, and J. Ye, *Tensor completion for estimating missing values in visual data*, IEEE Transactions on Pattern Analysis and Machine Intelligence, vol. 35, no. 1, pp. 208-220, 2013.
21. https://www.ehu.eus/ccwintco/index.php?title
22. https://engineering.purdue.edu/ biehl/MultiSpec/hyperspectral